Check for updates

Eu₃Ta₂ON₅: an *n* = 2 Ruddlesden–Popper ferromagnetic oxynitride with long-range ordered anion vacancies

Judith Oró-Solé,†[a] Jhonatan Ricardo Guarín,†[a] Carlos Frontera, [iD] *[a] Jaume Gàzquez,[a] Bernat Mundet,[b] Josep Fontcuberta [iD] *[a] and Amparo Fuertes [iD] *[a]

The new compound Eu₃Ta₂ON₅ with an *n* = 2 Ruddlesden–Popper structure has been prepared by solid state reaction between EuN, Eu₂O₃ and Ta₃N₅ at 1200 °C under N₂. It crystallizes in the *I*4/*mmm* space group with unit cell parameters *a* = 3.98240(1) Å and *c* = 20.42020(6) Å and has anion vacancies in central A-site layers of the perovskite blocks, where tantalum is in a square pyramidal coordination polyhedron with composition [TaO₀.₅N₄.₅] and europium is 8-coordinated. The perovskite blocks intergrow with [EuO₀.₅N₀.₅] NaCl-type layers of the Ruddlesden–Popper structure. Electron Energy Loss spectrum imaging shows a mixed Eu²⁺/Eu³⁺ valence with preferred occupation of Eu³⁺ in the 8-coordinated sites. Magnetic susceptibility measurements are consistent with the formal composition Eu²⁺₂Eu³⁺Ta⁵⁺₂ON₅ and indicate ferromagnetic order of Eu²⁺ ions below *T*_C = 20 K. Interestingly, despite the oxynitride containing non-magnetic Eu³⁺ ions (⁷F₀), the Curie temperature is found to be much larger than in related Eu₂TiO₄ and Eu₃Ti₂O₇ Ruddlesden–Popper compounds (≈9–10 K), which is attributed to the covalency-reinforced Eu²⁺–N/O–Eu²⁺ superexchange interactions.

Introduction

Simple perovskite oxynitrides ABO₃₋ₓNₓ -where A is an alkaline earth metal or rare earth metal and B is a transition metal- have been widely investigated because of their electronic and photocatalytic properties.[1] There are numerous examples of compounds with different combinations of cations and anion stoichiometries, and some paradigmatic materials are non-toxic pigments La₁₋ₓCaₓTaO₂₋ₓN₁₊ₓ,[2] BaTaO₂N and SrTaO₂N with high dielectric permittivity,[3] EuNbO₂N that shows colossal magnetoresistance at low temperature,[4] and LaTiO₂N that is a photocatalyst for water splitting.[5] Compounds with more complex structures are less common, and include magnetic double or triple perovskites such as La₂MnTaO₅N,[6] Ba₂MnWO₄.₄₂N₁.₅₈[7] or Eu₃Ta₃O₃.₆₆N₅.₃₄,[8] and polar hexagonal perovskite BaWON₂.[9] Perovskite related Ruddlesden–Popper oxynitrides AX(ABX₃)ₙ (X = O,N), formed by intergrowth of n perovskite blocks with a rock salt AX layer, have been reported as a few examples restricted to aluminum, tantalum and niobium at the B sites. Existing *n* = 1 members for alkaline

earth cations at A sites are Sr₂TaO₃N, Ba₂TaO₃N[10] and Sr₂NbO₃N.[11] Lanthanide derivatives were initially reported by Marchand for aluminum, R₂AlO₃N (R = La, Sm, Nd),[12] and more recently the tantalum compounds R₂Ta(O,N)₄ (R = La, Nd, Sm, Eu) have been discovered.[13] To the best of our knowledge the only reported *n* = 2 compounds are Sr₃Nb₂O₅N₂[11] and Eu₃Ta₂O₃N₄.[14] The strontium niobium compound was prepared using a solid state reaction at room pressure under NH₃ at 1050 °C, and crystallizes in the aristotype space group for Ruddlesden–Popper phases, *I*4/*mmm*. The europium tantalum phase was obtained in the form of single crystals by ammonothermal synthesis at 797 °C and 170 MPa. It was described as a europium mixed valence compound of detailed composition Eu³⁺₂Eu²⁺Ta₂O₃N₄, with a distorted symmetry *P*4₂/*mnm* and cell parameters *a* = 5.7278(1), *c* = 19.8149(5) Å.

Reported perovskite oxynitrides of europium show ferromagnetic order of Eu²⁺ *S* = 7/2 spins at low temperatures. EuNbO₂N, EuTaO₂N[4] and EuWO₁₋ₓN₂[15] show Curie temperatures up to 12 K, and Ruddlesden–Popper *n* = 1 Eu₂TaO₂.₈N₁.₂ orders below 8 K.[13] Additionally the Nb and W perovskites show colossal magnetoresistances at low temperatures, originating from the coupling between the carrier spins of the transition metal and the localized Eu spins.

Here we report the new *n* = 2 Ruddlesden–Popper oxynitride Eu²⁺₂Eu³⁺Ta₂ON₅ that has been prepared by a solid-state reaction between EuN, Eu₂O₃ and Ta₃N₅ at room pressure, under

[a]Institut de Ciència de Materials de Barcelona (ICMAB-CSIC), Campus UAB, 08193 Bellaterra, Spain. E-mail: amparo.fuertes@icmab.es
[b]Institut Català de Nanociència i Nanotecnologia (ICN2), Campus UAB-08193 Bellaterra, Barcelona, Spain
† These authors contributed equally to this work.

N_2 at 1200 °C, and shows a different crystal structure and richer Eu^{2+} contents than early reported $Eu^{3+}_2Eu^{2+}Ta_2O_3N_4$.[14] The differences in anion composition and crystal chemistry between these two compounds are due to the drastic changes in the synthesis conditions, as $Eu^{3+}_2Eu^{2+}Ta_2O_3N_4$ was obtained at much lower temperature and under high pressure conditions, starting with Ta, Eu, NaN_3 and NaOH.[14] Rietveld refinement of synchrotron X-ray diffraction data and integrated differential phase contrast imaging indicate that tantalum is in square pyramidal coordination analogously to the nitrides $R_3B_2N_6$ (R = La, Ce, Pr; B = Nb, Ta),[16] resulting from long-range ordered anion vacancies in the central europium layer of the perovskite blocks. The new compound represents the first example of a stoichiometric anion deficient oxynitride perovskite. Magnetization measurements show that Eu^{2+} ions, that are concentrated at the NaCl-type layers, are ferromagnetically ordered below 20 K. The Curie temperature is significantly larger than reported for Eu^{2+} perovskite-related oxides, where T_C has been found to be lower than 10 K. It will be argued that the ordering of magnetic Eu^{2+} and non-magnetic Eu^{3+} ions and the reinforced Eu–N/O–Eu superexchange interactions account for this remarkable observation.

Experimental

Synthetic procedures and chemical characterization

Black $Eu_3Ta_2ON_5$ samples of 100 mg were prepared by solid state reaction between Eu_2O_3 (Sigma-Aldrich 99.9%), EuN (Materion, 99.9%) and Ta_3N_5 at 1200 °C under N_2 gas (Air Liquide, 99.9999%) using one single treatment of 3 hours at this temperature. Ta_3N_5 was prepared by reaction of Ta_2O_5 (Sigma-Aldrich 99.99%) with NH_3 (Carburos Metálicos 99.9%) at 850 °C during several cycles of 15 hours with intermediate regrinding, using a flow rate of 600 cm^3 min^{-1}. Eu_2O_3 was treated at 900 °C under vacuum of 10^{-3} torr during 12 hours for dehydration. The reactants were weighed, mixed and pelletized in a glove box under recirculating Ar. The pellets were placed in molybdenum crucibles covered by zirconium foil. Another crucible with zirconium was placed near the sample in the reaction tube to scavenge H_2O and O_2 impurities from the gas. The reaction tube was evacuated to 10^{-3} torr and purged three times with N_2 before heating at 300 °C h^{-1} up to the maximum temperature. The obtained samples were stable in air.

Nitrogen analyses were performed in a Thermo Fisher Scientific instrument heating the samples up to 1060 °C under O_2, using MgO, WO_3 and Sn as additives and atropine as reference standard.

Structural characterization

Laboratory X-ray powder diffraction patterns were obtained on capillary samples of diameter 0.3 mm using a Bruker D8 Advance A25 diffractometer in a Debye Scherrer configuration with Mo $K\alpha_1$ radiation (λ = 0.7093 Å). High resolution synchrotron X-ray powder diffraction (SXRPD) data were collected at room temperature on the same capillaries in the angular range

$2.0° \leq 2\theta \leq 60°$ at the MSPD beamline of the ALBA Synchrotron (Cerdanyola del Vallès, Spain),[17] using multi analyser detector and 30 keV energy that resulted in a wavelength of 0.41376 Å determined by refining SRM640d NIST Si standard. Rietveld analysis was performed using the program Fullprof.[18] Background refinement was performed by linear interpolation and data were corrected from absorption.

Electron diffraction patterns were taken in a JEOL 1210 transmission electron microscope operating at 120 kV using a double tilt side entry specimen holder with tilting angles ±60°/±30°. The samples were deposited in powder form on a copper grid coated by a Lacey carbon film with a continuous layer of ultrathin carbon film.

Atomic resolution images were obtained at the Joint Electron Microscopy Center at ALBA (Cerdanyola del Vallès, Spain) on a double-corrected Thermo Fisher Spectra 300 (S)TEM microscope operated at 200 kV. High-angle annular dark field (HAADF) images were acquired using a semi-convergence angle of 19.5 mrad. Integrated differential phase contrast scanning transmission electron microscopy (iDPC-STEM) method has also been used for imaging of all elements using the segmented Panther detector from Thermo Fisher. This imaging mode detects the deflection of the beam produced by the atomic electrostatic fields thus allowing to image simultaneously heavy and light atoms.[19] Electron Energy Loss Spectroscopy (EELS) spectra were collected in a continuum spectrometer equipped with a fast direct electron detection camera K3 from Gatan, using a collection angle of around 40 mrad, a probe current of around 90p A and a dwell time of 50 ms. A principal component analysis filter was used after acquisition to minimize the random noise of the EELS spectrum images. To improve the energy resolution, the beam was monochromated using an excitation of 0.6, a spot size of 14 and a 1µm diameter C1 condenser aperture. This leads to a zero-loss peak full width at half maximum of around 0.4 eV. EDX spectra were acquired using a four quadrant Super-X windowless silicon drift detector system and beam currents of ≈100–250 pA. The crystal composition was quantified using the Thermo Fisher Scientific Velox software, applying the Cliff–Lorimer approach with Brown–Powell ionization cross-section models.
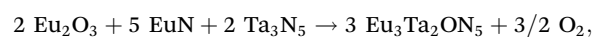
Magnetic measurements

Magnetic susceptibility measurements were performed on a Quantum Design SQUID magnetometer at temperatures between 2 and 300 K and magnetic fields of 25 Oe and 10 kOe. Magnetization-field loops were measured between −70 kOe and +70 kOe at temperatures below 50 K.

Results and discussion

Synthesis and structural study

The synthesis of the new anion deficient n = 2 Ruddlesden–Popper oxynitride takes place through the formal reaction:

$$2\ Eu_2O_3 + 5\ EuN + 2\ Ta_3N_5 \rightarrow 3\ Eu_3Ta_2ON_5 + 3/2\ O_2,$$

that involves an N/O ratio of 2.5 in the mixture of reactants. Under the synthesis conditions at 1200 °C in N_2, 2/3 of europium is reduced from +3 to the +2 oxidation state, with concomitant oxidation and loss of one O^{2-} anion per formula. The initial N/O ratio was tuned by changing the proportion of Eu_2O_3 and EuN in the mixture, until the optimal ratio $Eu_2O_3 : EuN : Ta_3N_5 = 0.45 : 8.1 : 2$ with N/O = 13.4 produced a sample free of impurities according to synchrotron X-ray powder diffraction data (Fig. 1).

Syntheses starting with N/O ratios below this value led biphasic samples with different proportions of the $n = 1$ member $Eu_2TaO_{2.37}N_{0.63}$. This phase is prepared at the same temperature but has a lower N/O stoichiometric ratio compared to $Eu_3Ta_2ON_5$,[13] hence the increase of N/O favours the formation of the $n = 2$ member. In the biphasic samples, $Eu_2TaO_{2.37}N_{0.63}$ was detected either in the X-ray diffraction patterns or as small intergrowth domains in the scanning transmission electron microscopy (STEM) images.

Electron diffraction patterns of $Eu_3Ta_2ON_5$ (Fig. 2) were indexed in a cell with $a \approx b \approx 3.97$ and $c \approx 20.54$ Å in the $I4/mmm$ aristotype space group, with reflection conditions: hkl, $h + k + l = 2n$; $hk0$, $h + k = 2n$; $0kl$, $k + l = 2n$; hhl, $l = 2n$; $00l$, $l = 2n$; $h00$, $h = 2n$. For some crystals, very weak additional reflections were observed in one of the $\langle 110 \rangle$ planes, that could be indexed in a $\sqrt{2}a_0 \times \sqrt{2}a_0 \times c_0$ superstructure with the orthorhombic space group $Amaa$ (no. 66), where a_0 and c_0 are the parameters of the $I4/mmm$ cell.

High-resolution HAADF-STEM imaging in combination with EDX and iDPC allowed mapping of the position of all atomic sublattices in real space. Fig. 3a shows a high-resolution HAADF-STEM image of a $Eu_3Ta_2ON_5$ crystal with the characteristic $n = 2$ Ruddlesden–Popper structure. EDX maps (Fig. 3b) showed no Eu/Ta intermixing, giving a ratio Eu/Ta of 2.8(2)/2; the nitrogen content of 7.56% determined by combustion analysis indicated 4.88 atoms per formula, close to the formal stoichiometry $Eu_3Ta_2ON_5$ where the oxygen content has
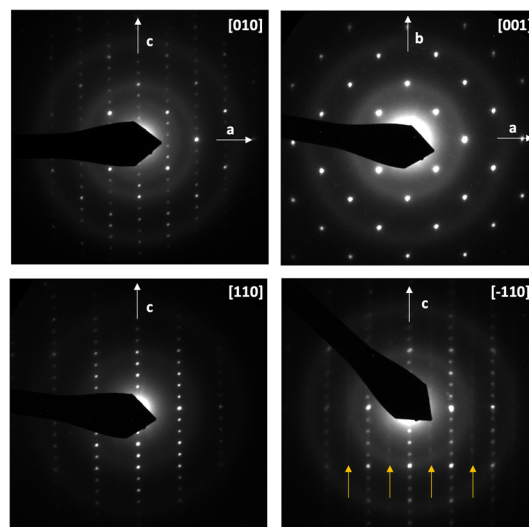

Fig. 2 Electron diffraction patterns of $Eu_3Ta_2ON_5$ along [010], [001] and [110] axes. Orange arrows indicate superstructure reflections observed in some crystals, that can be indexed in a $\sqrt{2}a_0 \times \sqrt{2}a_0 \times c_0$ unit cell.

been adjusted considering 6 anions. EDX spectra also indicated the presence of oxygen and nitrogen in the sample, but their quantitative analysis was not possible because of the large error observed for these light elements.

In order to probe the O and N sublattices, iDPC-STEM imaging mode was used, which is a direct phase imaging process that relies on atomic number. As the atomic number increases, the scattering intensity and signal brightness also rise. This imaging principle results in a linear relationship between the intensity in iDPC images and the atomic number.[19] In contrast, high-angle annular dark field (HAADF) images exhibit an approximate proportionality between intensity and the square of the atomic number. Consequently, iDPC-STEM offers greater information about lighter elements, which is highly valuable for investigating the O and N sublattices of $Eu_3Ta_2ON_5$. Notice that the iDPC contrast of the image of a crystallite oriented along [010] allows for the identification of all sublattices in $Eu_3Ta_2ON_5$. Remarkably, the planes signalled with an arrow show a much dimmer contrast due to an anion deficiency, consistent with a $n = 2$ Ruddlesden–Popper structure with 6 anions per formula and vacancies located between the two $[TaX_2]$ planes of the perovskite block, resulting in square pyramidal coordination of tantalum atoms.

Rietveld refinement of synchrotron X-ray powder diffraction data (Fig. 1) were performed in the $I4/mmm$ space group starting with the structural model of $La_3Ta_2N_6$ that has two crystallographically independent anions at 8g and 4e sites, corresponding respectively to equatorial and axial positions of the TaX_5 pyramids.[16] The refined cell parameters were $a = 3.98240$ (1), $c = 20.42024(6)$ Å, with agreement factors of $R_p = 6.90\%$, $R_{wp} = 8.95\%$, $\chi^2 = 6.35$ and $R_{Bragg} = 1.97\%$ (Table 1 and Fig. 4). Refinements were also performed in the $Amaa$ (no. 66) space group using a unit cell with parameters $\sqrt{2}a_0 \times \sqrt{2}a_0 \times c_0$ and three positions for the anions, but the observed Bragg R factor
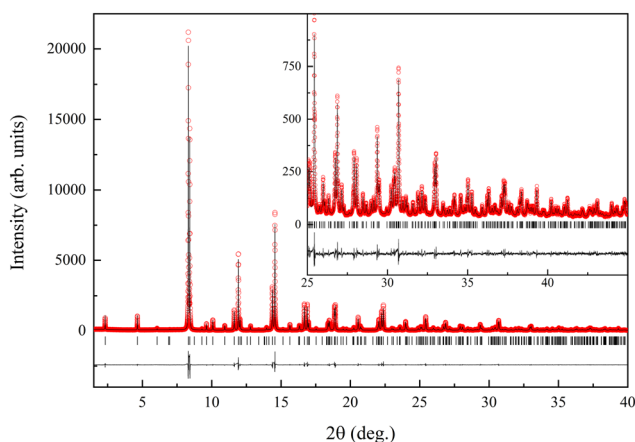

Fig. 1 Rietveld fit to synchrotron X-ray powder diffraction data ($\lambda = 0.41376$ Å) of $Eu_3Ta_2ON_5$, performed in the $I4/mmm$ space group with $a = 3.98240(1)$, $c = 20.42020(6)$ Å. The inset shows the high 2θ region enlarged.

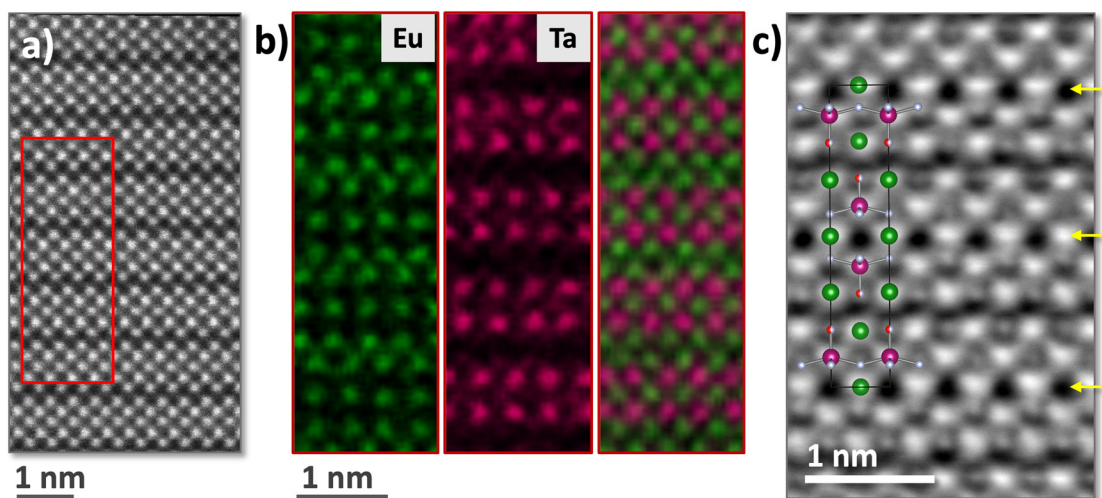**Fig. 3** (a) HAADF-STEM image of a $Eu_3Ta_2ON_5$ crystal along the [010] zone axis. The image shows an n = 2 Ruddlesden–Popper structure, with two perovskite blocks intergrowing with a rock salt-type layer. The inset shows the corresponding area for the elemental EDX maps. (b) From left to right, atomic resolution EDX maps of Eu (in green), Ta (in magenta) and a combined colour map. (c) iDPC image with the $Eu_3Ta_2ON_5$ structure overlay (Eu: green, Ta: magenta, O: red and N: light gray). Yellow arrows point to the planes in which the anion vacancies are located.

Table 1 Atomic coordinates in the $I4/mmm$ space group, cation and anion occupancies and isotropic temperature factors for $Eu_3Ta_2ON_5$ from the refinement to synchrotron X-ray powder diffraction data at 300 K using λ = 0.41376 Å[a]

Atom	Wyckoff site	x	y	z	B^b (Å²)	Occ. factor
Eu1	2b	0	0	0.5	0.44	1
Eu2	4e	0	0	0.31422(2)	0.65	1
Ta	4e	0	0	0.09922(3)	0.47	1
N1	8g	0	0.5	0.0738(3)	1.04(9)	1
O2/N2	4e	0	0	0.1910(3)	1.04	0.5/0.5

Bond length(Å)			
Ta–N1	2.0595(6) × 4	Ta–O2,N2 1.865(6)	
Eu1–N1	2.493(4) × 8		
Eu2–N1	3.036(5) × 4	Eu2–O2,N2 2.525(6)	
Eu2–O2,N2	2.8177(2) × 4		

[a] O/N occupation factors were fixed considering the predicted distribution using Pauling's second crystal rule. Refined cell parameters were a = 3.98240(1), c = 20.42024(6) Å. Agreement factors: R_p = 6.90%, R_{wp} = 8.95%, χ^2 = 6.35, R_{Bragg} = 1.97%. [b] B_{eq} in Å² is calculated for Eu and Ta atoms from refined anisotropic temperature factors (×10⁴): Eu1 β_{11} = β_{22} = 64(3) β_{33} = 3.1(2); Eu2 β_{11} = β_{22} = 120(4) β_{33} = 2.5(2); Ta β_{11} = β_{22} = 59(2) β_{33} = 3.9(1). The temperature factors were common for the two anion sites.
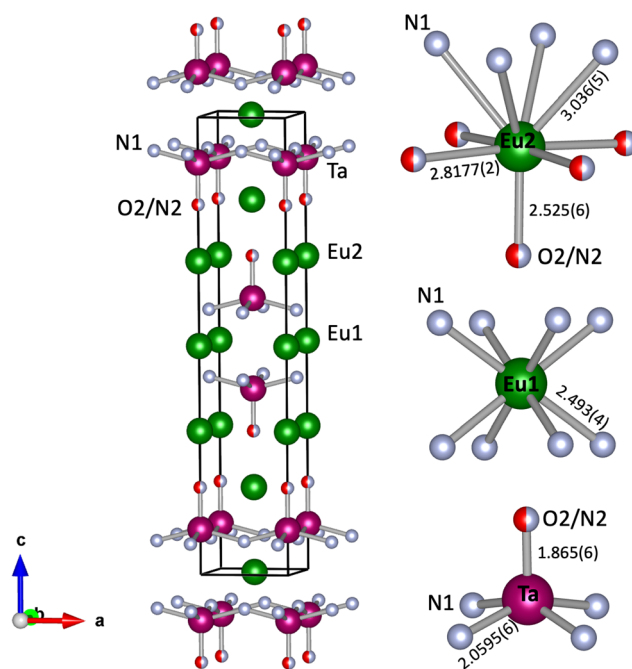

Fig. 4 Structural model in *the* $I4/mmm$ space group and cation coordination polyhedra of $Eu_3Ta_2ON_5$ showing bond distances.

was significantly larger than for the $I4/mmm$ model (5.06% *vs.* 1.97%).

The europium atoms in $Eu_3Ta_2ON_5$ show two well differentiated polyhedra with coordination numbers 8 and 9 for Eu1 at 2b and Eu2 at 4e sites respectively, and corresponding average bond distances of 2.493(4) and 2.871 Å. Considering the difference between both distances and the ionic radii of Eu^{3+} for CN = VIII (1.01 Å) and Eu^{2+} for CN = IX (1.30 Å),[20] the new oxynitride can be formally formulated as $Eu^{2+}{}_2Eu^{3+}Ta^{5+}{}_2ON_5$, a charge-ordered compound where Eu^{3+} occupies the 8-coordinated sites and Eu^{2+} ions are in the 9-coordinated sites.

The distribution of O and N in the 8g and 4e sites could not be determined from X-ray diffraction because this technique does not provide enough contrast between the two anions. Neutron powder diffraction is the optimal technique to investigate the anion ordering in oxynitrides, but for $Eu_3Ta_2ON_5$ the large absorption cross section of europium

would make difficult to obtain accurate information from these data. Pauling's second crystal rule (PSCR) can be used to predict the anion distribution in mixed anion compounds,[21,22] from the calculation of the bond strength sums (b) with the equation:

$$b = \sum_i \frac{z_i}{\nu_i},$$

where z_i and ν_i are the electrical charge and coordination number of each cation bonded to a given anionic position.

According to PSCR, the electrical charge of each anion (q) tends to compensate the strength of the electrostatic valence bonds from the cations (b). Considering the ordering of Eu^{3+} at 2b sites and Eu^{2+} at 4e sites, the calculated bond strength sums are 2.85 and 1.94 for the anions at 8g and 4e positions respectively, predicting the preferred occupancy of N atoms at the equatorial positions of the [TaX_5] pyramids. Accordingly, in the refinement we used fixed 100% occupancy of nitrogen on 8g sites and 50/50 N/O at 4e sites.

The observed equatorial Ta–N bond distance (2.0595(6) Å) is similar to those reported for $La_3Ta_2N_6$ and $Ce_3Ta_2N_6$ (2.053(3) and 2.0465(19) Å respectively).[16] In contrast, the Ta–O,N apical distance (1.865(6) Å) is slightly shorter than in the two nitrides (1.96(3) and 1.951(19) Å for $La_3Ta_2N_6$ and $Ce_3Ta_2N_6$ respectively). This difference is consistent with the mixed O/N occupancy at axial sites, according with the larger ionic radius of N^{3-} compared to O^{2-} (1.46 vs. 1.38 Å, both for CN = IV).[20]

EELS measurements provided detailed atomic scale information of the oxidation state of both Eu2 and Eu1 sites by analysing the energy onset of the Eu M4,5 edge. Fig. 5(a–c) shows a HAADF-STEM image of a $Eu_3Ta_2ON_5$ crystal and two EEL spectra from the crystallographic sites Eu2 and Eu1. The fine structure of the two Eu M4,5 spectra is clearly different, although the source is not as straight forward. For Eu^{2+} species the onset is lower in energy than that of the Eu^{3+} species.[23] If both Eu^{2+} and Eu^{3+} are present, EEL spectra typically display two peaks with the stronger one belonging to the dominant oxidation state. The thickness of the sample may also play an important role, as it widens the electron beam, it lowers the spatial resolution and increases the contribution of nearest unit cells,[24] which may be the reason of a presence of a Eu^{2+} signal in the spectra acquired from the Eu1 site, or of Eu^{3+} in the spectra acquired for the Eu2 site. Nonetheless, these EELS measurements support the preferred occupation of Eu^{2+} and Eu^{3+} ions in Eu2 and Eu1 sites, respectively, of $Eu_3Ta_2ON_5$.

Magnetic properties

The temperature-dependent magnetic susceptibility $\chi(T)$ (black symbols) and $\chi^{-1}(T)$ (red symbols) of $Eu_3Ta_2ON_5$, recorded at H = 5k Oe, are shown in Fig. 6. It can be appreciated that $\chi^{-1}(T)$ displays an appreciable bending, suggesting an additional temperature-dependent contribution other than the Curie–Weiss behavior. As indicated by the solid lines thorough the data, the susceptibility per mole can be well fitted by the contributions from $n_{Eu^{2+}}$ moles of Eu^{2+} ($S = 7/2$, $J = 7/2$), modelled as a Curie–Weiss law, and a small temperature-
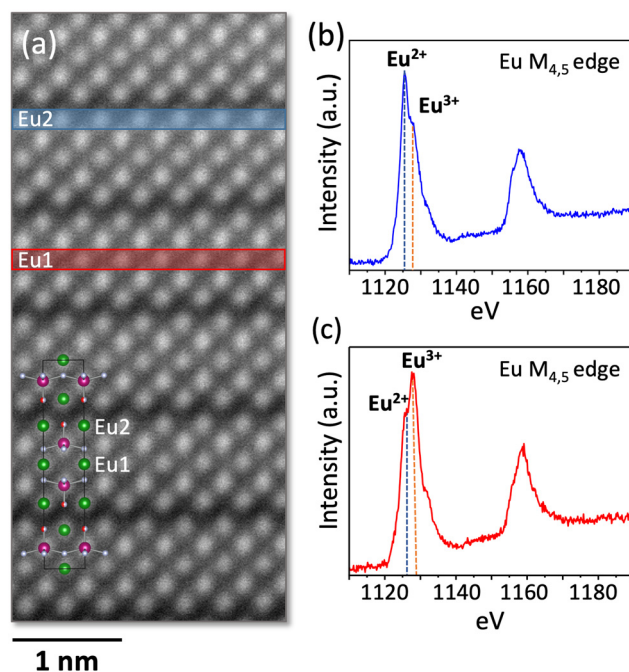

Fig. 5 (a) HAADF-STEM image of the $Eu_3Ta_2ON_5$ crystal along the [010] zone axis with the $Eu_3Ta_2ON_5$ structure overlay (Eu: green, Ta: magenta, O: red and N: light gray). (b) and (c) show the averaged EEL M4,5 spectra obtained from Eu2 and Eu1 sites of the $Eu_3Ta_2ON_5$ structure, marked in blue and red in (a), respectively.
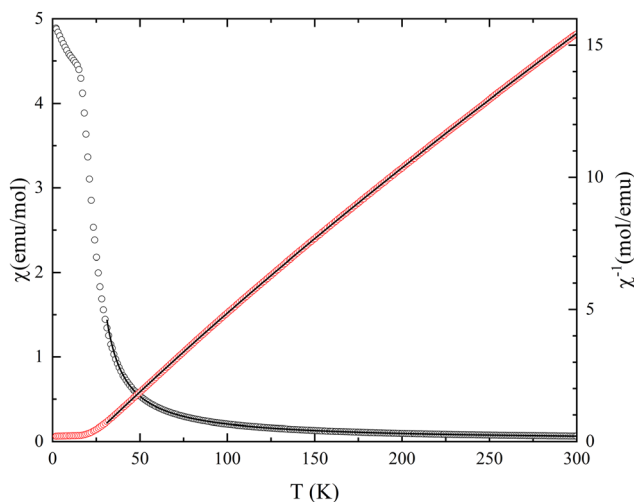

Fig. 6 Magnetic susceptibility $\chi(T)$ (left axis) and the reciprocal $\chi^{-1}(T)$, (right axis) recorded at 5 kOe. Solid lines are the results of the fit described in the text.

dependent Van Vleck contribution arising from $n_{Eu^{3+}}$ moles of Eu^{3+}, in addition to a background contribution (χ_0). Notice that although Eu^{3+} ground state is nonmagnetic ($^7F_0$, $S = 3$, $L = 3$, $J = 0$), thermal excitation to higher lying states (for instance the first one ($^7F_1$, $S = 3$, $L = 3$, $J = 1$) is only at about 46 meV[25]) shall produce an additional contribution to the magnetic susceptibility ($\chi_{Eu^{3+}}$), that will add to the Eu^{2+} contribution, and to

the diamagnetic contribution. Accordingly, the magnetic susceptibility per Eu ion can be expressed as:[8,13]

$$\chi(T) = n_{Eu^{2+}} \chi_{Eu^{2+}}(T) + n_{Eu^{3+}} \chi_{Eu^{3+}}(T) + \chi_0,$$

where:

$$\chi_{Eu^{2+}}(T) = \frac{N_A \mu_B{}^2 g_J{}^2 J(J+1)}{3k_B} \frac{1}{(T-\theta)} \left(\text{with } J = \frac{7}{2} \text{ and } g_J = 2\right),$$

$$\chi_{Eu^{3+}}(T) = \frac{\sum\limits_{J=0}^{6} (2J+1)\chi_J(T) \exp[-\lambda J(J+1)/k_B T]}{\sum\limits_{J=0}^{6} (2J+1) \exp[-\lambda J(J+1)/k_B T]},$$

with:

$$\chi_J(T) = \frac{N_A \mu_B{}^2 g_J{}^2 J(J+1)}{3k_B T} + \frac{2N_A \mu_B{}^2 (g_J-1)(g_J-2)}{3\lambda},$$

and $g_J = 3/2$, except g_0 that equals $2 + L = 2 + S = 5$.[26,27]

Fitting to experimental inverse susceptibility was done by varying $n_{Eu^{2+}}$, $n_{Eu^{3+}}$, θ and χ_0, while fixing $\lambda/k_B = 531.5$ K (equivalent to an energy splitting, $\lambda = 46$ meV, between the non-magnetic ground state of Eu^{3+} and its first excited state),[13,26] as well as the effective paramagnetic moment of Eu^{2+}. From the fit, we obtain $n_{Eu^{2+}} = 1.98$, $n_{Eu^{3+}} = 1.02$, $\theta = 20.2$ K and $\chi_0 = 4.6 \times 10^{-3}$ emu mol^{-1}. These results are quite consistent with chemical analysis and crystal structure results, that suggest 2 Eu^{2+} and 1 Eu^{3+} per formula. The extrapolated Curie–Weiss temperature is $\theta > 0$ (≈ 20 K), indicating the prevalence of ferromagnetic interactions.

In agreement with the susceptibility data of Fig. 6, the M(H) loops (Fig. 7) develop a ferromagnetic-like shape at $T \leq$ 20 K. At 2 K the saturation magnetization is about $14\mu_B$ per f. u., which is fully consistent with the presence of two ferromagnetically ordered Eu^{2+} ions per f.u in this oxynitride. The ferromagnetic ordering occurring at $T \approx 20$K is evidenced in the zero-field-cooling and field-cooling susceptibility data recorded at low field (inset in Fig. 7), that show a perceptible hysteresis.

The most remarkable feature of these results is that the Curie temperature (≈ 20 K) is significantly larger than those reported for similar systems, such as Ruddlesden–Popper $n = 1$ Eu_2TiO_4 and $n = 2$ $Eu_3Ti_2O_7$,[25,28] where T_C is around 9–10 K. To rationalize the observed dramatic enhancement of T_C in $Eu_3Ta_2ON_5$, it is worth to compare these results with isostructural $Eu_3Ti_2O_7$, that for this purpose is described as a sequence of $EuTiO_3$ (perovskite-type) and Eu_2TiO_4 (K_2NiF_4-type, rock salt) blocks .[25] We recall that, as argued above, the non-magnetic Eu^{3+} ions in $Eu_3Ta_2ON_5$ occupy Eu1 sites equivalent to those in $EuTiO_3$ structure and the magnetic Eu^{2+} ions occupy Eu2 sites as in Eu_2TiO_4. Therefore, the magnetic interactions in $Eu_3Ta_2ON_5$ are analogous to those for Eu_2TiO_4.

Fig. 8 illustrates the most relevant magnetic nearest-neighbor (nn) (J_{11} and J_{12}) and next-nearest-neighbor (nnn) magnetic interactions (J_{21}) in Eu_3TaON_5. Notice that we omit magnetic interactions involving Eu^{3+} as this ion is nonmagnetic. Here, we follow the nomenclature of Chien *et al.*[25] who
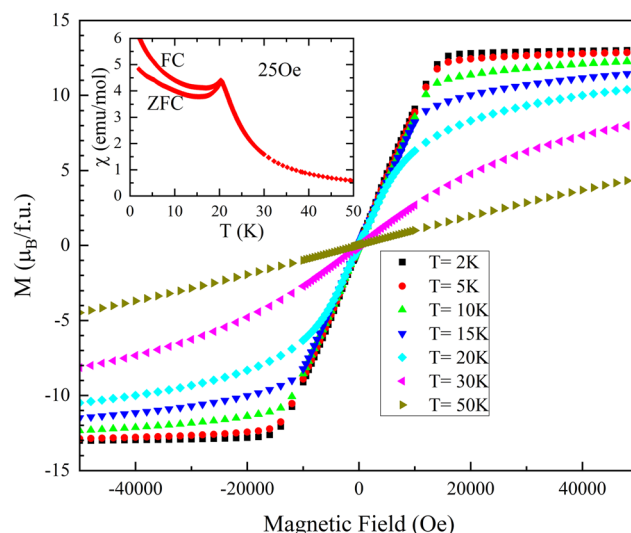

Fig. 7 Magnetization loops recorded at several temperatures (indicated) up to ± 5 T. Inset: zero field-cooled/field-cooled magnetization *vs.* temperature measured under 25 Oe applied magnetic field.
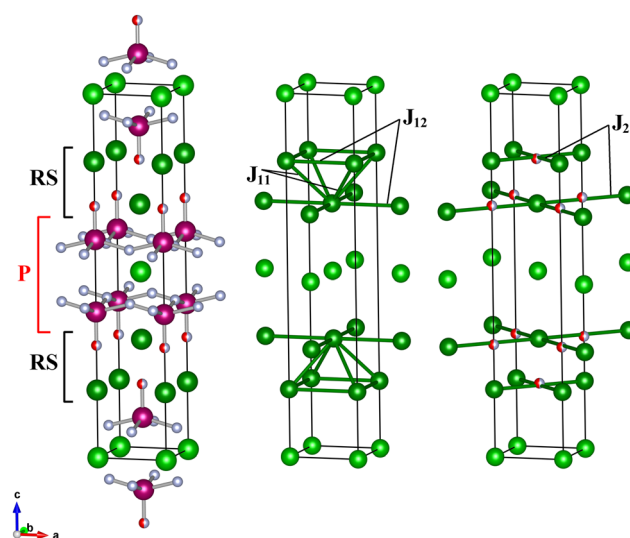

Fig. 8 Sketch of the structure and the most relevant nn (J_{11} and J_{12}) and nnn (J_{21}) magnetic interactions in $Eu_3Ta_2ON_5$. Ta, N and O atoms are represented by magenta, light gray and red spheres respectively; Eu^{3+} and Eu^{2+} are shown as light and dark green spheres respectively. The two structural blocks for Eu are labelled as P, (perovskite) and RS (rock salt, K_2NiF_4-type blocks). For comparison with ref. 25, the structure has been shifted by (0.5,0.5,0) with respect to Fig. 4.

employed a mean field approach to describe the T_C of $Eu_3Ti_2O_7$ in terms of the nn and nnn magnetic interactions (eqn (19) in ref. 25). The model can be easily adapted to the present case by keeping only interactions involving Eu^{2+} ions; namely J_{11}, J_{12} and J_{21}. It follows that:

$$T_C = \frac{16S(S+1)(J_{11} + J_{12} + J_{21})}{\kappa_B}$$

where S (= 7/2) is the Eu^{2+} spin and κ_B is the Boltzmann constant. Structural data indicates that nn Eu–Eu distances in Eu_2TiO_4 (3.814 Å)[25] are only slightly shorter (1.3%) than in $Eu_3Ta_2ON_5$ (3.864 Å). Similarly, the next-nearest-neighbor nnn Eu–O–Eu distance in Eu_2TiO_4 (5.465 Å)[25] are also slightly shorter (1.8%) than nnn Eu–(N/O)–Eu distance in $Eu_3Ta_2ON_5$ (5.566 Å). Therefore, taking the nn interactions J_{11} and J_{12} as in Eu_2TiO_4 ($\approx$0.11 K[25]) and using the expression above, we derive the nnn Eu–(N/O)–Eu interaction $J_{21} \approx 0.13$ K that is much (×4) larger than J_{21} in Eu_2TiO_4 (0.037 K).

We note that the $4f^7$ electrons of Eu^{2+} have well localized wave functions with tiny overlapping with neighboring Eu^{2+} ions. It follows that the direct 4f–4f interaction is negligible. Instead, as proposed long ago by Goodenough[29] and Kasuya,[30] intra-atomic 4f–5d intermixing offers a mechanism to propagate magnetic interactions. The 4f–5d intermixing is dictated by the relative position of the 4f and 5d orbitals, the latter being determined by the crystal field.[25,29,30] As the coordination polyhedra of Eu^{2+} in $Eu_3Ta_2ON_5$ and Eu_2TiO_4 have rather similar bond lengths, it can be suspected the 4f–5d mixing in these compounds to be similar. As the nn distances in both compounds differ only by some 1.5%, it follows that the nn Eu–Eu interactions (J_{11}, J_{12}) should be also similar, justifying the assumption made above.

Similarly, as the Eu–Eu nnn distances in both structures are also similar (within 1.8%), we conclude that the reinforced ferromagnetic Eu–Eu interaction results from the fact that the Eu–(N/O)–Eu hybridization is much enhanced. This can be explained by the higher hybridization (lower electronegativity of 2p(N) orbitals compared to 2p(O)) with 4f–5d orbitals of Eu. Enhanced ferromagnetic interactions induced by the large covalency of Mn–N bonds have also been observed in $Ba_2MnWO_{4.42}N_{1.58}$ oxynitride.[7]

In short, the selective occupation of Eu^{3+} and Eu^{2+} in the two A sites of $Eu_3Ta_2ON_5$ precludes magnetic dilution, that would be present if both cations would occupy the same site, and the reinforced hybridization of Eu–(N/O)–Eu bonds strengthens the ferromagnetic superexchange. On the other hand, this selective occupation implies the absence of bridging magnetic ions in the perovskite block (see Fig. 8). It follows that ferromagnetic order takes place basically within the Eu^{2+}-containing bilayers of the rock-salt block. Therefore, a natural question arises: if the Eu^{2+} bilayers are magnetically decoupled, why do they appear similarly magnetically aligned in the magnetic measurements shown above? Tiny magnetic interactions between them may exist, either *via* direct dipolar coupling or *via* the presence of a small fraction of Eu^{2+} at the perovskite positions. However, none of those mechanisms, nor the combination of them, seem to be compatible with the observed large T_C ($\approx$20 K). Alternatively, the internal field associated to the Eu^{2+} ordering, may induce mixing of $J = 1$ and $J = 0$ in the ground state of Eu^{3+} (^7F_J) mimicking the role of an external field which is responsible for the temperature-independent paramagnetism of Eu^{3+}, with the consequent induction of a magnetic moment in an otherwise non-magnetic ion. The induced moment in Eu^{3+} may be responsible for the interlayer ferromagnetic coupling, as observed in $Eu_{1-x}Y_xMnO_3$.[31] Therefore, the possibility arises that the two RS blocks of Eu^{2+} in the $Eu_3Ta_2ON_5$ structure spontaneously order separately but are further aligned due to the magnetic applied field. Elucidating this possibility would only be possible by characterizing the magnetic order at zero field (*e.g.* by muon spectroscopy).

Conclusions

The new $n = 2$ Ruddlesden–Popper oxynitride $Eu_2^{2+}Eu^{3+}Ta_2ON_5$ has been prepared by a solid state reaction between EuN, Eu_2O_3 and Ta_3N_5 during 3 hours under N_2 at 1200 °C. It crystallizes in the $I4/mmm$ space group, with cell parameters $a = 3.98240(1)$ and $c = 20.42024(6)$ Å. Contrast inverted STEM iDPC images show long range ordered anion vacancies in the Eu layers between the TaX_2 planes of the perovskite blocks, which decrease the coordination number of the transition metal from 6 to 5 anions, analogously to reported rare earth nitrides $R_3B_2N_6$ (R = La, Ce, Pr; B = Nb, Ta). The anion vacancies generate two different environments for europium, with 8-coordinated Eu^{3+} located between the TaX_2 planes and 9-coordinated Eu^{2+} in rock-salt layers. The magnetization data of $Eu_2^{2+}Eu^{3+}Ta_2ON_5$ shows ferromagnetic order of Eu^{2+} $S = 7/2$ spins below $T_C =$ 20 K. The selective occupation of Eu^{3+} and Eu^{2+} in the two sites gives rise to Eu^{3+} magnetically inert perovskite blocks that alternate with rock-salt blocks of ferromagnetic Eu^{2+} bilayers, where the presence of nitrogen at the anion sites leads to stronger Eu–(N/O)–Eu superexchange interactions and a record ordering temperature. The nitride introduction in the $n = 2$ Ruddlesden–Popper structure allows electronic and chemical orders and subsequent tailoring of magnetic interactions. New magnetic properties may emerge by further modification of the N/O ratio that certainly will modify the balance between the two europium oxidation states.

Author contributions

J. O. S. and J. R. G.: investigation, formal analysis. B. M.: investigation. C. F. and J. G: investigation, formal analysis, methodology, writing. A. F. and J. F: conceptualization, supervision, writing.

Data availability

The data used in this publication are available from the author on reasonable request. The synchrotron X-ray powder diffraction data are available through the following link **https://doi.org/10.20350/digitalCSIC/17261**.

Conflicts of interest

There are no conflicts to declare.

Acknowledgements

References

1 A. Fuertes, *APL Mat.*, 2020, **8**, 020903.

2 M. Jansen and H. P. Letschert, *Nature*, 2000, **404**, 980.

3 Y. Kim, P. M. Woodward, K. Z. Baba-Kishi and C. W. Tai, *Chem. Mater.*, 2004, **16**, 1267.

4 A. B. Jorge, J. Oró-Solé, A. M. Bea, N. Mufti, T. T. M. Palstra, J. A. Rodgers, J. P. Attfield and A. Fuertes, *J. Am. Chem. Soc.*, 2008, **130**, 12572.

5 A. Kasahara, K. Nukumizu, G. Hitoki, T. Takata, J. N. Kondo, M. Hara, H. Kobayashi and K. Domen, *J. Phys. Chem. A*, 2002, **106**, 6750.

6 K. Ishida, C. Tassel, D. Watabe, H. Takatsu, C. M. Brown, G. J. Nilsen and H. Kageyama, *Inorg. Chem.*, 2021, **60**, 8252.

7 J. Oró-Solé, C. Frontera, J. R. Guarín, J. Gàzquez, B. Mundet, C. Ritter, J. Fontcuberta and A. Fuertes, *Chem. Mater.*, 2024, **36**, 10267.

8 J. R. Guarín, C. Frontera, J. Oró-Solé, J. Gàzquez, C. Ritter, J. Fontcuberta and A. Fuertes, *Inorg. Chem.*, 2023, **62**, 17362.

9 J. Oró-Solé, I. Fina, C. Frontera, J. Gàzquez, C. Ritter, M. Cunquero, P. Loza-Alvarez, S. Conejeros, P. Alemany, E. Canadell, J. Fontcuberta and A. Fuertes, *Angew. Chem., Int. Ed.*, 2020, **59**, 18395.

10 F. Pors, R. Marchand and Y. Laurent, *Ann. Chim.*, 1991, **16**, 547.

11 G. Tobías, J. Oró-Solé, D. Beltrán-Porter and A. Fuertes, *Inorg. Chem.*, 2001, **40**, 6867.

12 R. Marchand, *C. R. Acad. Sci., Ser. C*, 1976, **282**, 329.

13 J. R. Guarín, C. Frontera, J. Oró-Solé, B. Colombel, C. Ritter, F. Fauth, J. Fontcuberta and A. Fuertes, *Chem. Mater.*, 2024, **36**, 5160.

14 N. Cordes, M. Nentwig, L. Eisenburger, O. Oeckler and W. Schnick, *Eur. J. Inorg. Chem.*, 2019, 2304.

15 M. Yang, J. Oró-Solé, A. Kusmartseva, A. Fuertes and J. P. Attfield, *J. Am. Chem. Soc.*, 2010, **132**, 4822.

16 L. Cario, Z. A. Gál, T. P. Braun, F. J. Di Salvo, B. Blaschkowski and H.-J. Meyer, *J. Solid State Chem.*, 2001, **162**, 90.

17 F. Fauth, I. Peral, C. Popescu and M. Knapp, *Powder Diffr.*, 2013, **28**, S360.

18 J. Rodríguez-Carvajal, *Phys. B*, 1993, **192**, 55.

19 I. Lazić, E. G. T. Bosch and S. Lazar, *Ultramicroscopy*, 2016, **160**, 265.

20 R. D. Shannon, *Acta Crystallogr., Sect. A*, 1976, **99**, 751.

21 L. Pauling, *J. Am. Chem. Soc.*, 1929, **51**, 1010.

22 A. Fuertes, *Inorg. Chem.*, 2006, **45**, 9640.

23 M. Mizumaki, Y. Saitoh, A. Agui, K. Yoshii, A. Fujimori and S. Nakamura, *J. Synchrotron Radiat.*, 2001, **8**, 440.

24 R. F. Egerton, *Electron Energy-Loss Spectroscopy in the Electron Microscope*, Springer, New York, NY, 2011.

25 C.-L. Chien, S. DeBenedetti, F. De and S. Barros, *Phys. Rev. B*, 1974, **10**, 3913.

26 M. Adruh, E. Bakalbassis, O. Kahn, J. C. Trobe and P. Porcher, *Inorg. Chem.*, 1993, **32**, 1616.

27 O. Khan, *Molecular Magnetism*, VHC Pubs, New York, 1993, pp. 46–48.

28 J. E. Greedan and G. J. McCarthy, *Mater. Res. Bull.*, 1972, **7**, 531.

29 J. B. Goodenough, *Magnetism and Chemical Bond*, Interscience, New York, 1963.

30 T. Kasuya, *IBM J. Res. Dev.*, 1970, **14**, 214.

31 A. Skaugen, E. Schierle, G. van der Laan, D. K. Shukla, H. C. Walker, E. Weschke and J. Strempfer, *Phys. Rev. B: Condens. Matter Mater. Phys.*, 2015, **91**, 180409(R).